CFD-based study on one- and two-point statistics of wall pressure fluctuations

Nan Hu*

German Aerospace Center (DLR), Lilienthalplatz 7, 38108 Braunschweig, Germany

This paper presents a study on the statistics of wall pressure fluctuations with the so-called TNO-Blake model. The focus is on the statistics which have essential importance for the surface structural vibration, such as the one-point and wavenumber-frequency spectra, the coherence lengths and the convection velocity of the wall pressure field. The turbulent-boundary-layer (TBL) parameters which needed for the model are provided by RANS calculations. Calculations were carried out for zero pressure gradient flows with two velocities and an adverse pressure gradient flow, illustrating Reynolds number and pressure gradient effects. The effects on the one-point spectra, especially the contribution from different wall-normal positions across TBL, and on two-point statistics are discussed. Furthermore, the impact of different formulations for the velocity spectrum and moving axis spectrum on the wall pressure statistics is demonstrated.

I. Introduction

Turbulent boundary layer (TBL) induced wall pressure fluctuations are a major noise source for many engineering applications, such as aircraft cabin noise and wind turbine noise. Generally, noise generation is related to both one- and two-point statistics of the wall pressure fluctuations. The former represents the source power, and the latter determines the noise generation efficiency.

The major research focus on the one-point statistics is the wall pressure one-point spectra. Based on an extensive measurement database, Goody[1] proposed a wall pressure spectra model for zero pressure gradient (ZPG) flows. The model reveals the Reynolds number effect on the wall pressure spectra, characterized by an extended overlap range with increasing Reynolds numbers. Recently, more investigations have been made on flows under pressure gradients.[2–4] In general, adverse pressure gradients (APG) affect the wall pressure fluctuations stronger than favorable pressure gradients (FPG). The APG increases the spectral peak magnitude and steepens the spectral roll-off at medium frequencies.[5–7] The contribution from different wall-normal positions across the turbulence boundary layer (TBL) is also of interest which helps understand the physical mechanism of the wall pressure fluctuations production. Blitterswyk and Rocha[8] and Szőke *et al.*[9] measured the coherence between the velocity fluctuations across TBL and the wall pressure fluctuations for low Reynolds number flows, indicating that the buffer layer contributes significantly to the wall pressure fluctuations over the entire frequency range. Blitterswyk and Rocha showed that the log region becomes more important with an increasing Reynolds number.

The two-point statistics describe the space-time characteristics which can be represented by the wavenumber-frequency spectra. The important parameters for the wall pressure field are the coherence length and convection velocity. With these parameters, the wavenumber-frequency spectra can be formulated.[10,11] A larger coherence length denotes a stronger correlated wall pressure field, which generally increases the noise generation. Hu[12] showed that the coherence length increases with an increasing Reynolds number. The APG reduces the streamwise coherence length while increasing the spanwise length. The Reynolds number and APG effects are more pronounced in the streamwise direction. The convection velocity has great importance for the flow-induced surface vibration, especially for velocities close to a coincidence between the structure and the wall pressure field.[13,14] Smol'yakov[15] proposed a convection velocity model for ZPG flows. It has been found that the APG significantly reduces the velocity magnitude. This effect was considered in the model proposed by Catlett[3] through modifying the Smol'yakov model.

*Research scientist, Department of Technical Acoustics, Institute of Aerodynamics and Flow Technology, nan.hu@dlr.de

The wall pressure fluctuations can be analytically calculated with the TNO-Blake model.[16,17] The needed TBL parameters, such as the mean shear velocity, Reynolds stress, length and time scales, can be obtained by CFD results. The model provides solutions for one-point spectra, wavenumber-frequency spectra and, furthermore, physical insights. Contributions from different wall-normal positions across TBL for the wall pressure fluctuations can be obtained. Panton and Linebarger[18] and Peltier and Hambric[19] demonstrated the pressure gradient effects on the source distribution. Furthermore, the Reynolds number effect on the wall pressure one-point spectra can be predicted by the model.[18]

In the present work, wall pressure fluctuations are calculated with TNO model for two ZPG cases and one APG case. The above introduced one- and two-point statistics, such as the one-point spectra, source distributions, coherence lengths and convection velocities, are obtained. Reynolds number and APG effects are discussed. Furthermore, the impact of the length and time scales on the wall pressure fluctuations is demonstrated.

II. Methods and mean flow conditions

Pressure fluctuations within an incompressible TBL are governed by a Poisson equation. The sources consist of the mean-shear term and the turbulence-turbulence term. Neglecting the turbulence-turbulence term, the wall pressure fluctuations can be calculated with the TNO-Blake model:[16,17]

$$\Phi_{pp}(k_1,k_3,\omega) = 4\rho_0^2\frac{k_1^2}{k^2}\int_0^\delta \left[\frac{\partial u_1(x_2)}{\partial x_2}\right]^2 \overline{u_2'^2}(x_2)\Lambda_2(x_2)\Phi_{22}(k_1,k_3,x_2)\phi_m(\omega-k_1u_c(x_2))e^{-2|k|x_2}\,\mathrm{d}x_2, \quad (1)$$

where ρ_0 is the air density, k_i is wavenumber component with the subscript $1,2,3$ denoting the streamwise, wall-normal and spanwise directions, respectively. The wavenumber $k^2 = k_1^2 + k_3^2$. The quantity of $\overline{u_2'^2}$ is the Reynolds stress of u_2' component and u_1 is the local mean velocity. The wavenumber spectrum $\Phi_{22}(k_1,k_3)$ of u_2' can be formulated using von Kármán spectrum,[20] expressed as:

$$\Phi_{22}(k_1,k_3) = \frac{4}{9\pi}l_s^2\beta_1\beta_3\frac{(\beta_1 l_s k_1)^2 + (\beta_3 l_s k_3)^2}{[1+(\beta_1 l_s k_1)^2 + (\beta_3 l_s k_3)^2]^{7/3}}\,, \quad (2)$$

where l_s is the characteristic length of the velocity fluctuations and $\beta_{1,3}$ are the anisotropy factor for the respective flow directions. There are different values of β suggested. For example, $\beta_1 = 1$ and $\beta_3 = 0.9$ were suggested by Fischer *et al.*,[21] and $\beta_1 = 1$ and $\beta_3 = 0.75$ by Stalnov *et al.*[22] The ratio of β_1/β_3 determines the level of turbulence anisotropy and a larger value represents a a higher anisotropy level. For an isotropic spectra, $\beta_{1,3} = 1$.

The length scale l_s can be obtained based on the RANS result, using

$$l_s = \frac{c_l}{C_\mu}\frac{\sqrt{k_t}}{\omega_d}, \quad (3)$$

where k_t is the turbulent kinetic energy and ω_d is the specific turbulent dissipation rate. The constant $C_\mu = 0.09$ and c_l is estimated to be 0.54.[23] As an alternative to Eq. (3), l_s can be calculated based on the mixing length l_m, reads[17,24]

$$l_s = \frac{l_m}{\kappa}\frac{\Gamma(1/3)}{\sqrt{\pi}\,\Gamma(5/6)}, \quad (4)$$

with $\kappa = 0.41$ and $l_m = 0.085\delta\tanh(0.41x_2/0.085\delta)$.

The parameter Λ_2 in Eq. (1) is the double-sided integral correlation length of u_2' in the wall-normal direction, which is obtained with $\Lambda_2 = 2\Lambda_{22}$. The parameter Λ_{22} is the single-sided integral length and equal to $0.747l_s$ for the Von Karman spectrum.[20,21]

The function $\phi_m(\omega - k_1u_c)$ is the moving axis spectrum which describes the temporal turbulence decay during convection. Taylor's frozen turbulence hypothesis[25] is used in most cases for calculating wall pressure spectra,[20,21,24] expressed with the Dirac delta function:

$$\phi_m(\omega - k_1u_c) = \delta(\omega - k_1u_c). \quad (5)$$

Parchen[17] suggested the following expression including the temporal decay,

$$\phi_m(\omega - k_1u_c) = \frac{1}{\alpha\sqrt{\pi}}\exp(-(\omega - k_1u_c)/\alpha)\,, \quad (6)$$

with $\alpha = 0.05u_c/\Lambda_{22}$.

The moving axis spectrum can also be expressed with a time scale, τ_s, obtained from RANS. Based on an assumption of the temporal decay with $\exp(-\tau/\tau_s)$ in space-time domain as suggested in Refs.,[26,27] the moving axis spectrum can be expressed as:[28]

$$\phi_m(\omega - k_1 u_c) = \frac{\tau_s}{\pi(1 + (\omega - k_1 u_c)^2 \tau_s^2)}\,, \tag{7}$$

with

$$\tau_s = c_\tau \frac{l_s}{\sqrt{k_t}}\,, \tag{8}$$

where the pre-factor c_τ needs to be empirically determined. By comparing the streamwise coherence of wall pressure fluctuations, Hu *et al.*[28,29] suggested $c_\tau = 1.2$ and 2.5. The former value was determined with a wall pressure fluctuations simulation for a low Reynolds number ZPG flow, and the latter for an aircraft fuselage flow at cruise conditions. The time scale τ_s is an indicator for the turbulence decay rate and a larger τ_s represents a slower decay. For frozen turbulence, $\tau_s \to \infty$.

The turbulent convection velocity u_c is set equal to the local mean velocity in this work based on the results by Kim[30] and Alámo and Jiménez,[31] which showed that both velocities are essentially the same except for the region very close to the wall.

Two cases for ZPG flow over a flat plate and one APG case are investigated in this work. For the APG case, the APG flat plate flow was produced with a 400 mm chord length NACA 0012 airfoil, installed 120 mm above the plate.[4] The leading edge of the NACA airfoil was located at $x_1 = 850$ mm ($x_1 = 0$ is the leading edge of the plate model), and the geometric angle of attack was 10° with the rotation axis at 41% of the chord length. Two-dimensional (2D) RANS calculations for the three cases were conducted using the differential Reynolds stress model with a g-equation[32].[33] For details about the measurement and RANS calculation, the reader is referred to Hu and Herr[4] and Hu *et al.*[33] The boundary layer parameters for the selected cases are summarized in Table 1, which were determined at $x_1 = 1210$ mm on the flat plate. The results from RANS are in good agreement with the measurement results, except for the boundary layer thickness for the APG case which is too thin compared to the measurement result. This is probably due to the 2D RANS which cannot account for the increased impact of the open-jet shear layer due to the airfoil on the boundary layer flows.[34,35]

Fig. 1 shows the boundary layer profiles of parameters which are needed for the TNO-Blake model in x_2/δ and x_2^+ next to it. The mean velocity profile and Reynolds stress of u_2' show good agreement between the measurement and RANS results. There is an error that occurred in the sublayer of the RANS result for the APG case, evidenced by the disagreement with the sublayer profile based on the law of the wall, see Fig. 1(b). Note, that this error reduces the friction velocity, u_τ. The value of u_τ shown in Table 1 for the APG case is estimated by fitting the log- and wake-region profiles to the measurement results. This value is also used for all wall unit plots in this paper. The Reynolds stress profiles and the APG effect on the Reynolds stress are well predicted by the RANS calculation, see Figs. 1(c,d). However, the Reynolds stress is over-predicted for all cases at about $x_2/\delta < 0.5$ and under-predicted at a larger x_2/δ.

Figs. 1(e,f) show the length scale, calculated with Eqs. (3-4). Two methods have similar results at $x_2/\delta < 0.2$, see Fig. 1(e). At a larger x_2/δ, the result obtained using Eq. (3) shows difference between different flow conditions, whereas there is no difference for the cases calculated with Eq. (4). A better view of the length scale in the near-wall region can be gained with the results plotted in wall units, see Fig. 1(f). Significantly different values can be observed between two methods at $x_2^+ < 30$. The length scale obtained with Eq. (3) drops rapidly in this region, whereas Eq. (4) leads to a linear decrease approaching the wall.

Figs. 1(g,h) show the time scale, calculated with $c_\tau = 2.5$. The results show that τ_s increases with a larger distance to the wall. Both ZPG cases have a similar trend and the value of τ_s at a given x_2/δ is significantly larger than that for the APG case. When τ_s is plotted in wall units, the value for the APG case is larger than that for the ZPG cases at $x_2^+ < 200$.

III. Results

The wall pressure spectra are calculated based on Eq. (1). The input parameters can be determined differently, as introduced in the last section. All three flow cases are calculated with a reference setting where the input variables are defined as follows: anisotropic velocity spectrum Φ_{22} is applied with a larger anisotropy factor, i.e. $\beta_1 = 1$ and $\beta_3 = 0.75$.[22] The length scale l_s is determined using Eq. (4) with the help of the mixing length l_m. This choice is based on the predicted wall pressure spectrum, which shows significantly better agreement with the measurement result at high frequencies compared to the one calculated using Eq. (3). Based on the prediction, ϕ_m is calculated using Eq. (7) with $c_\tau = 2.5$.

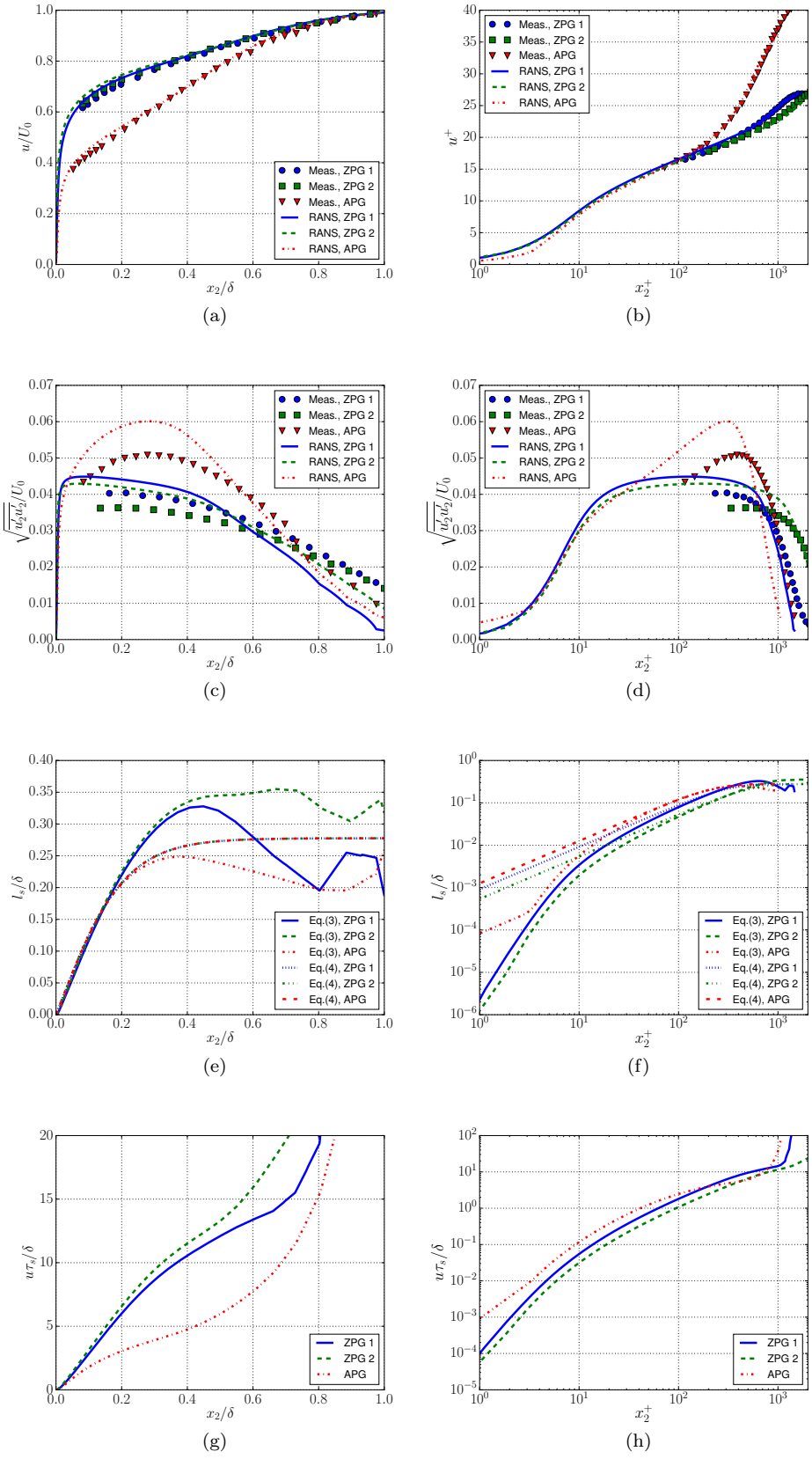

Figure 1: Boundary layer profiles, (a, b) mean velocity; (c, d) Reynolds stress of u_2' component; (e, f) length scale; (g, h) time scale.

Table 1: Boundary layer parameters.

	U_0 (m/s)	δ (mm)	δ^* (mm)	θ (mm)	H δ^*/θ	u_τ (m/s)	Re_θ $= U_0\theta/\nu$	Re_τ $= u_\tau\delta/\nu$
ZPG 1, RANS	30.1	20.0	3.34	2.42	1.38	1.13	4730	1468
ZPG 1, Measurement	30.2	19.7	3.51	2.49	1.41	1.13	4889	1439
ZPG 2, RANS	58.8	17.9	2.9	2.15	1.35	2.14	8209	2487
ZPG 2, Measurement	58.7	18.5	3.13	2.28	1.37	2.08	8685	2499
APG, RANS	30.4	19.7	5.05	2.93	1.72	0.83	5784	1062
APG, Measurement	30.4	28.7	7.68	4.39	1.75	0.75	8670	1388

To demonstrate the impact of the length and time scale on predicted results, the wall pressure fluctuations are calculated for the ZPG 1 case with Φ_{22} and ϕ_m determined using different formulations.

A. One-point statistics

The wall pressure spectrum is calculated by integrating $\Phi_{pp}(k_1, k_3, \omega)$ over k_1 and k_3,

$$\Phi_{pp}(\omega) = 4\rho_0^2 \int_0^\delta \int_{-\infty}^{\infty} \int_{-\infty}^{\infty} \frac{k_1^2}{k^2} \left[\frac{\partial u_1(x_2)}{\partial x_2}\right]^2 \overline{u_2'^2}(x_2)\Lambda_2(x_2)\Phi_{22}(k_1, k_3, x_2) \phi_m(\omega - k_1 u_c(x_2))e^{-2|k|x_2}\, \mathrm{d}k_1\, \mathrm{d}k_3\, \mathrm{d}x_2. \quad (9)$$

The integration over k_i is performed prior to x_2 for determining contributions (integral spacing of $\Delta x_2 = 0.1\%\delta$) from different wall-normal positions. Figs. 2(a-c) show the calculated wall pressure spectra compared to the measured results,[4] along with the contributions from selected positions. Overall, a good prediction is achieved for all three cases. Although the magnitude is slightly underpredicted, the spectral shape is in good agreement with the measurement. The calculated spectrum for the ZPG 2 case shows an extended mid-frequency range with a constant slope (overlap region) compared to the ZPG 1 case, see Fig. 2(d), which is known as the Reynolds number effect on the wall pressure spectra.[1] The effect of APG that increases the peak magnitude and steepens mid-frequency roll-off is well represented. Note, that the measured high-frequency spectrum for the ZPG 2 case was contaminated by the Helmholtz resonance measured with a pinhole-mounted sensor.

The individual contributions from different wall-normal positions illustrate that small eddies close to the wall dominate the high-frequency wall pressure fluctuations and also significantly contribute to lower frequencies. The larger eddies further away from the wall contribute to the wall pressure spectra at lower frequencies. However, the results show that the contribution from $x_2/\delta = 0.4$ is negligible for the ZPG cases. The APG increases the importance of the larger eddies for the wall pressure fluctuations, indicated by the larger magnitude of the contributed spectra at $x_2/\delta = 0.15$ and 0.4, see Figs. 2(c,d). The increased contribution from these positions raises the peak magnitude of the wall pressure spectrum and results in a steeper mid-frequency roll-off compared to the ZPG case. Fig. 2(d) shows that the peak position of the individual spectra contributed from the same x_2/δ position does not depend on the Reynolds number and pressure gradient. For example, all spectral peaks for $x_2/\delta = 0.01$ occur at $\omega\delta/U_0 \simeq 3.5$. Note, the same x_2/δ position has different x_2^+ values for different flow conditions. For the ZPG cases, x_2^+ increases with an increasing Reynolds number from 15 to 25 for $x_2/\delta = 0.01$. This indicates that the spectrum contributed from the same x_2^+ shifts to a higher frequency for a larger Reynolds number flow.

A better view of the source distribution can be gained by gathering all contributions across the TBL. Fig. 3 shows the frequency-space map of the source distribution for the wall pressure spectrum referenced to the maximum magnitude of each frequency among all contributions. This source map reveals the importance of different wall-normal positions. The result shows that the main contribution to ZPG wall pressure fluctuations comes from $x_2/\delta < 0.2$, see Figs. 3(a,b). The wall unit plots demonstrate that the buffer layer ($5 < y^+ < 30$) dominates the contribution for the wall pressure fluctuations over the entire frequency range. This result agrees with the findings of Blitterswyk and Rocha[8] and Szőke *et al.*[9] who measured coherence between wall pressure and TBL velocity fluctuations, indicating the source distribution. The log region contributes mainly to medium frequencies and the x_2^+ value of the source ridge increases with decreasing frequency. The source range is extended to a larger x_2^+ for a larger Reynolds number (the ZPG 2 case), corresponding to the extended log region. Consequently, the log region becomes more important due to its increased source weighting, e.g. see the source distribution at

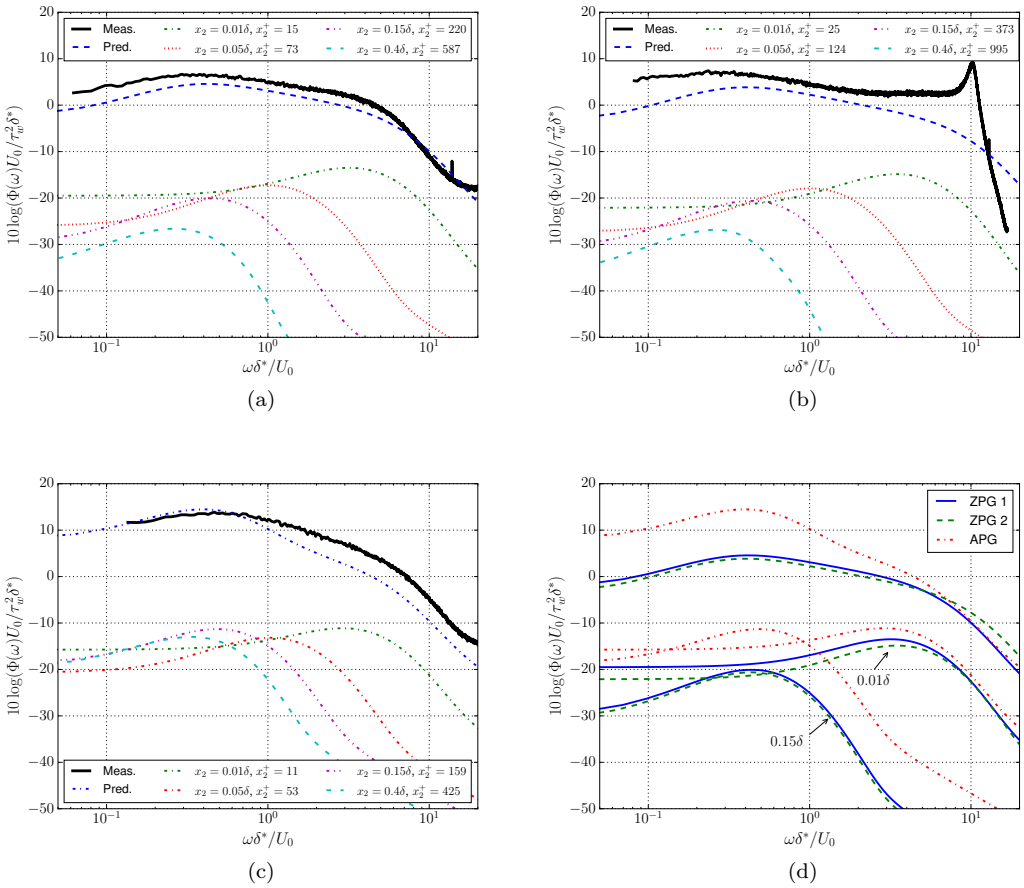

Figure 2: Wall pressure spectra including contributions from different wall-normal positions, (a) ZPG 1; (b) ZPG 2; (c) APG; (d) comparison between different cases.

$\omega\delta^*/U_0 = 0.5$ between Figs. 3(c,d). This observation agrees with the measured coherence by Blitterswyk and Rocha, which indicated increased importance of the log region for a larger Reynolds number flow. Furthermore, the source ridge shifts to a larger $\omega\delta^*/U_0$ with an increasing Reynolds number, which may explain the increased spectral overlap range, see Fig. 2(d). For example, the overlap region ends at $\omega\delta^*/U_0 \simeq 4$ and $\omega\delta^*/U_0 \simeq 7$ for the ZPG 1 and ZPG 2 cases, respectively. From these frequencies upwards, the spectra drop faster. Figs. 3(d,e) show that the peak of the ridge is located at $x_2^+ \simeq 12$ for these frequencies. This indicates that the end of the overlap region corresponds to the x_2^+ location of the source ridge. Thus, the source ridge shift to a larger $\omega\delta^*/U_0$ due to increasing Reynolds numbers may extend the overlap range of the ZPG wall pressure spectrum.

Figs. 3(c,f) show that the outer layer ($x_2^+ > 110$, $x_2/\delta > 0.1$) becomes more important for the APG case and dominate the contribution below $\omega\delta^*/U_0 \simeq 0.6$. According to Eq. (9), the increased contribution from the outer layer is due to the increased quantities of $\partial u_1/\partial x_2$ and $\overline{u_2'^2}$, refer to Figs. 1(a-d). The obtained result is essentially consistent with the finding of Jaiswal *et al.*[36] who calculated the source distribution of wall pressure fluctuations for an airfoil flow under adverse pressure gradients. There is some difference between the two calculations at low frequencies. The present result shows that the buffer layer contributes significantly at frequencies $\omega\delta^*/U_0 < 2$ which was not the case in Ref.[36] This is probably because Jaiswal *et al.* calculated the wall pressure spectrum using frozen turbulence assumption which could significantly reduce the contribution of the buffer layer to low frequencies. This phenomenon will be demonstrated in the following discussion.

The effects of the length and time scales on wall pressure fluctuations are investigated by using different formulations of Φ_{22} and ϕ_m. Fig. 4(a) shows the wall pressure spectra calculated with isotropic turbulence, i.e. $\beta_{1,3} = 1$, or anisotropic turbulence but using l_s obtained according to Eq. (3). Compared to the calculation with anisotropic turbulence, the spectral level is slightly increased with isotropic turbulence, agreeing with the result by Grasso.[24] The spectrum calculated with l_s obtained using Eq. (3) drops much faster at medium frequencies compared to the reference spectrum. This is due

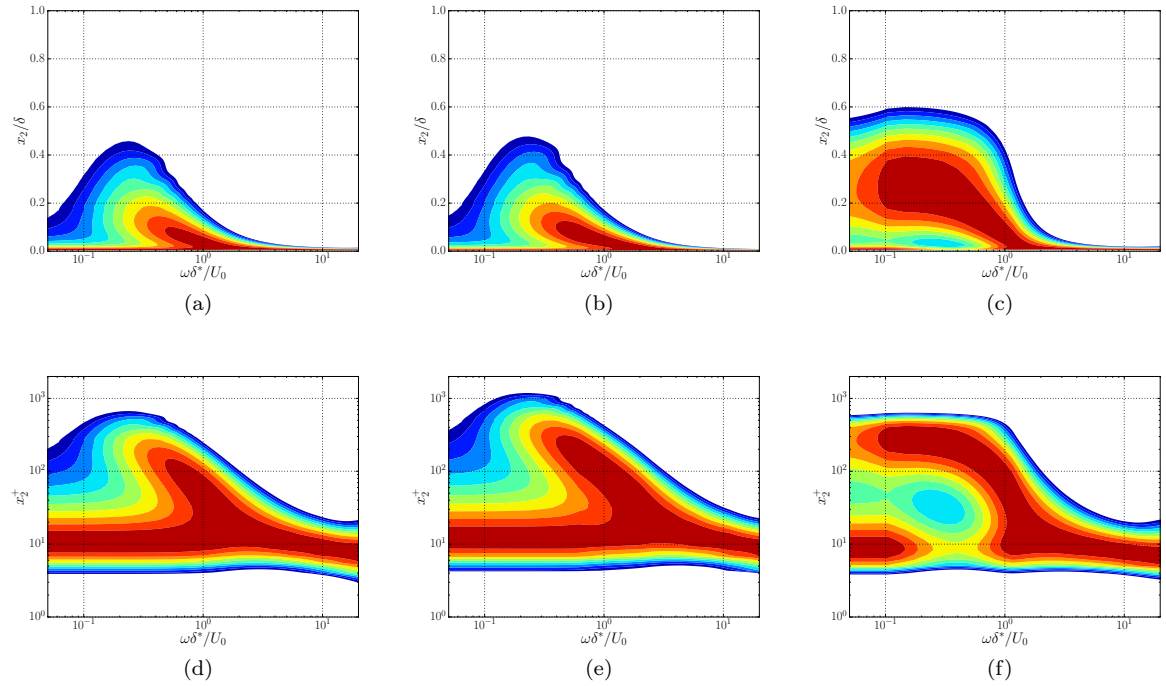

Figure 3: Source distribution, level between -10 dB and 0 dB with an interval of 1 dB (same scale applied to all following contour plots), (a,d) ZPG 1; (b,e) ZPG 2; (c,f) APG.

to the significantly reduced contribution from the near-wall area which is related to the smaller value of l_s at $x_2^+ < 100$, refer to Fig. 1(f).

Fig. 4(b) shows the result for the moving axis spectrum ϕ_m calculated using Eq. (7) with $c_\tau = 1.2$, Eq. (6) and Eq. (5). The function ϕ_m represents the temporal turbulence decay. In general, a larger τ_s leads to a slower turbulence decay. With $\tau_s \to \infty$, Eq. (7) becomes to Eq. (5), representing frozen turbulence. A smaller c_τ gives a smaller τ_s, resulting in a faster turbulence decay. The result obtained with Eq. (6) is comparable with the frozen turbulence case, indicating the formulation corresponding to a very large τ_s.

The result shows that the turbulence decay increases the low- and high-frequency magnitude of individual contributions while losing the peak magnitude slightly. Hu *et al.*[28] argued that considering the turbulence decay, ϕ_m changes from the Dirac delta function to a broader form. Thus, the energy of the frozen turbulence spectrum is spread into neighboring frequencies. In this case, from the peak to lower and higher frequencies. This phenomenon significantly increases the contribution from the near-wall region to lower frequencies and raises the low-frequency slope flatter than the classic ω^2.[1,16]

Figs. 5 and 6 show the source distribution for the ZPG 1 case plotted in wall units, calculated with the settings as discussed in Fig. 4. The result for the isotropic turbulence approach is comparable with the anisotropic turbulence case. For the case with l_s calculated with Eq. (3), the outer layer becomes significantly more important due to the loss in the contribution of the near-wall area. The turbulence decay mainly changes the contribution from the buffer layer to lower frequencies ($\omega\delta * /U_0 < 1$), see Fig. 6. The smaller the turbulence decay, the irrelevant the buffer layer for lower frequencies.

B. Two-point statistics

Fig. 7 shows the calculated wavenumber-frequency spectra at $\omega\delta^*/U_0 = 1$ using Eq. (1) with the reference setting. The convection ridge is well identified. The spectra are comparable for the ZPG cases and become broader in the k_1 direction in APG, agreeing with the literature.[37]

The convection velocity $U_c(\omega)$ can be determined based on the wavenumber-frequency spectra, using $U_c(\omega) = \omega/k_1$. The value of k_1 denotes the peak position of the convection ridge. The obtained convection velocity is consistent with the result derived from a LES dataset,[34] see Fig. 8 . The APG reduces the velocity magnitude which is also represented in the prediction. There are some discrepancies at low frequencies, where the peak position is predicted at a lower frequency compared to the LES result.

The streamwise and spanwise coherence lengths are calculated by the integration of the coherence

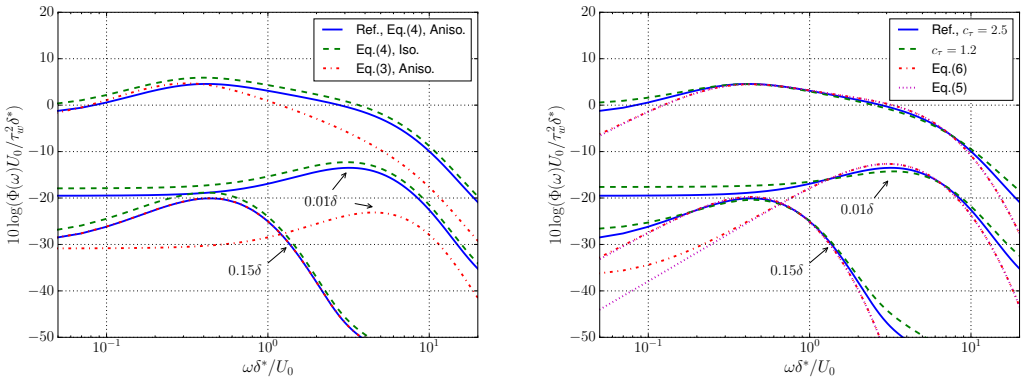

(a) (b)

Figure 4: Wall pressure spectra for the ZPG 1 case, (a) different formulations of Φ_{22}; (b) different formulations of ϕ_m.

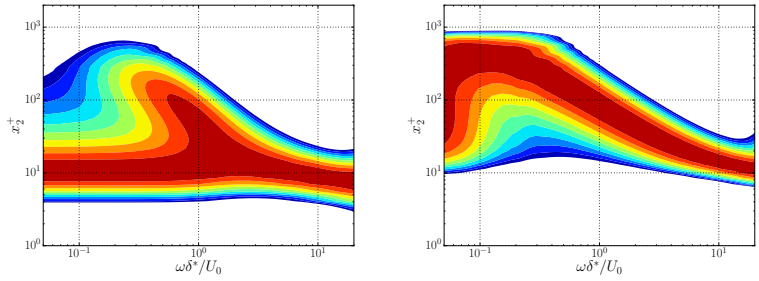

(a) (b)

Figure 5: Source distribution for the ZPG 1 case with Φ_{22} using, (a) l_s calculated with Eq. (4), isotropic turbulence; (b) l_s calculated with Eq. (3), anisotropic turbulence.

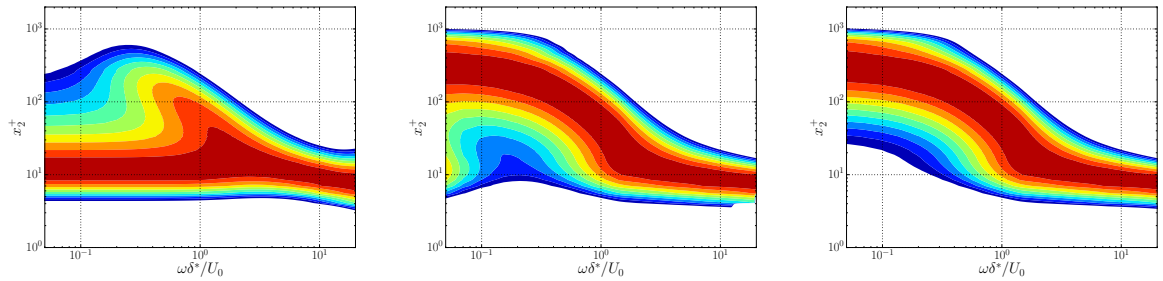

(a) (b) (c)

Figure 6: Source distribution for the ZPG 1 case with ϕ_m calculated using, (a) Eq. (7), $c_\tau = 1.2$; (b) Eq. (6); (c) Eq. (5).

spectrum in the respective directions,

$$l_{1,3}(\omega) = \int_0^\infty \Gamma_{pp}(r_{1,3}, \omega)\, \mathrm{d}r_{1,3}\,, \tag{10}$$

where the coherence can be determined by taking the 2D Fourier Transforms of the wavenumber spectra,

$$\Gamma_{pp}(r_1, r_3, \omega) = \int_{-\infty}^{\infty}\int_{-\infty}^{\infty} \Phi_{pp}(k_1, k_3, \omega) \exp(-ik_1 r_1) \exp(-ik_3 r_3)\, \mathrm{d}k_1\, \mathrm{d}k_3. \tag{11}$$

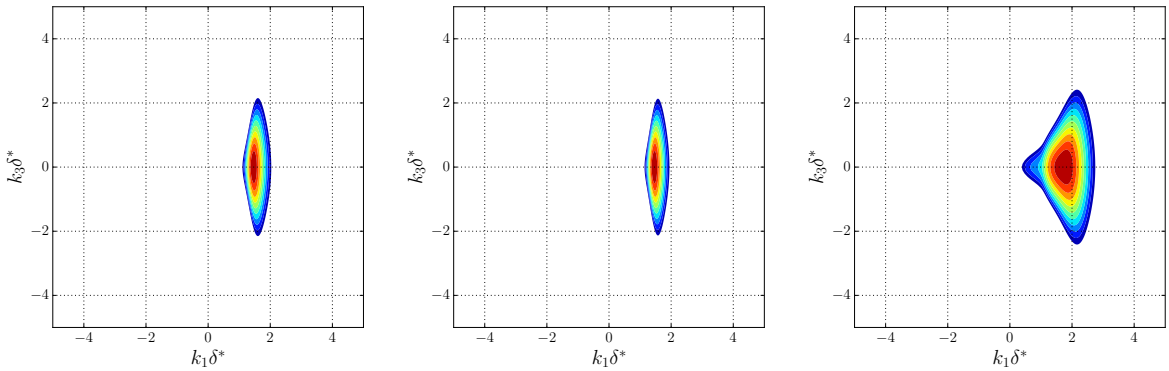

Figure 7: Wavenumber spectra at $\omega\delta^*/U_0 = 1$, (a) ZPG 1; (b) ZPG 2; (c) APG.

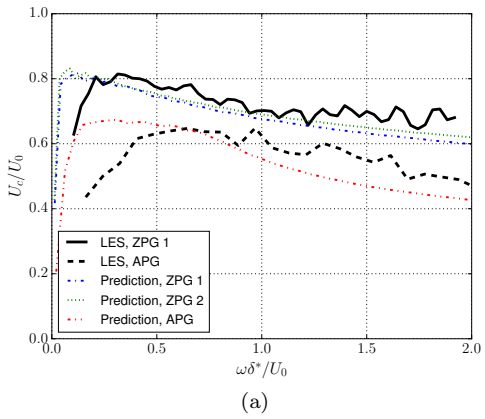

Figure 8: Convection velocity.

Fig. 9 shows the calculated coherence lengths compared to the measured results.[12] Overall, good prediction accuracy is achieved for both directions and all test cases. The spanwise coherence length is slight over-predicted. The magnitude of the streamwise coherence length is well predicted, except for a slight over-prediction at medium frequencies. The effects of APG and Reynolds number are more pronounced in the streamwise direction. The streamwise coherence length increases with an increasing Reynolds number and reduces significantly due to APG. The change of the streamwise coherence length corresponds to the difference of the time scale values in x_2/δ, see Fig. 1(g). As discussed in the last section, a smaller τ_s increases the temporal turbulence decay during convection, resulting in a smaller streamwise coherence length. Furthermore, Fig. 2(d) shows that the spectra produced from the same x_2/δ contribute mainly to the same frequencies for all test cases. Thus, it may be concluded that the smaller τ_s values in x_2/δ for the APG case reduce the streamwise coherence length. Note, that the τ_s values for the ZPG 2 case are slightly larger than the ZPG 1 case, see Fig. 1(g), which may lead to a small increase in the streamwise coherence length. Another factor that may affect the coherence lengths in both directions is the source distribution. Figs. 3(d,e) show that the log region becomes more important for the wall pressure fluctuations with an increasing Reynolds number, which also means that the importance of the buffer layer drops. The reduced importance of the buffer layer may increase the coherence lengths because the wall pressure fluctuations contributed from the buffer region decay faster and have a smaller correlated structure.

The effect of different input parameters on the calculated wall pressure fluctuations is investigated in the same way as is done for the one-point statistics. Figs. 10 and 11 show the results of the convection velocity and coherence length for the ZPG 1 case, calculated with different settings. Note, that the spectra above 1 kHz for the frozen turbulence case (Eq. (5)) are cut because the numerical noise increases significantly, probably related to applying the Dirca delta function. The obtained convection velocity is comparable between all settings. It seems that the velocity magnitude increases slightly with an

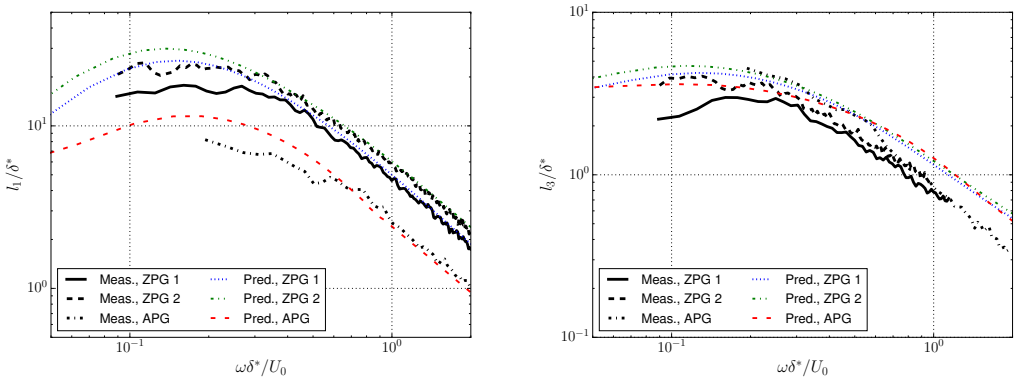

(a) (b)

Figure 9: Coherence length, (a) streamwise direction; (b) spanwise direction.

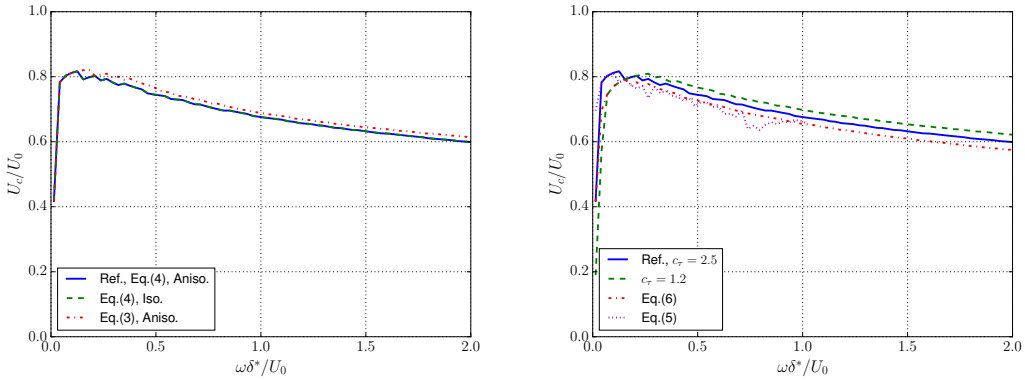

(a) (b)

Figure 10: Convection velocity for the ZPG 1 case, (a) different formulations of Φ_{22}; (b) different formulations of ϕ_m.

increasing turbulence decay, see Figs. 10(b).

Fig. 11(a) shows that the coherence length calculated using l_s obtained with Eq. (3) increases in both directions. This is due to the significant reduced contribution from the near-wall area, refer to Figs. 4(a) and 5(b). The wall pressure fluctuations contributed from positions closer to the wall have a smaller coherence length because the eddies in this region are smaller and decay faster. Surprisingly, there is almost no difference between the results for anisotropic and isotropic turbulence. Generally, one may expect that with anisotropy turbulence the spanwise coherence length would reduce due to the smaller vortex size in the spanwise direction. To understand this unexpected result, the anisotropy effect on the velocity spectra and the resulting pressure spectra for $x_2/\delta = 0.05$ and $\omega\delta^*/U_0 = 1$ is analyzed as an example that represents the effect for other positions and frequencies as well. Figs. 12(a,d) show the vortex stretching in the velocity wavenumber spectra, indicated by the extended contour in the k_3 direction for the anisotropic turbulence approach. Note, that a broader wavenumber spectrum represents reduced coherence in the space domain. However, the stretching effect disappears after multiplying with the factor, $k_1^2/k^2 e^{-2|k|x_2}$ in Eq. (1). Consequently, the anisotropy effect on the obtained wall pressure wavenumber spectra cannot be identified.

Fig. 11(b) illustrates the effect of turbulence temporal decay on the coherence length, which mainly affects the streamwise coherence length. A smaller decay (larger c_τ) increases the streamwise coherence length over the whole frequency range, except for the frozen turbulence case (Eq. (5)). A further increased magnitude compared to the case calculated with Eq. (6) occurs only at low-frequencies. This is probably because Eq. (6) provides a very small decay effect close to frozen turbulence, as indicated in Figs. 4(b) and 6(b,c). Furthermore, the reduced turbulence decay decreases the contribution from the near-wall area to low frequencies, which may result in the increased low-frequency magnitude in the spanwise

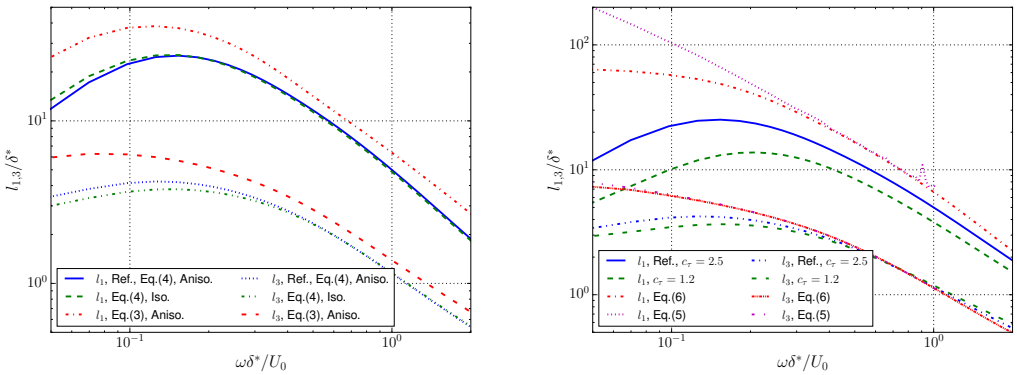

(a) (b)

Figure 11: Coherence length for the ZPG 1 case, (a) different formulations of Φ_{22}; (b) different formulations of ϕ_m.

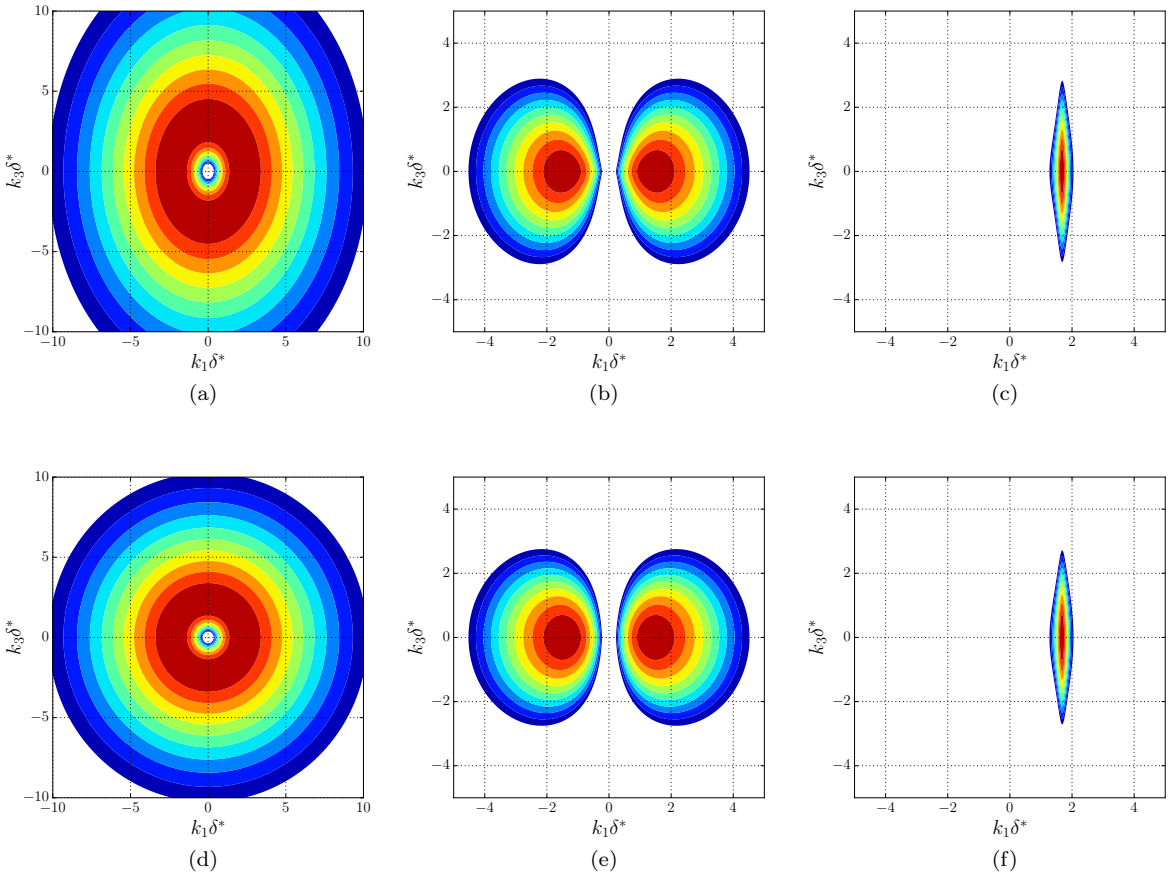

(a) (b) (c)

(d) (e) (f)

Figure 12: Velocity and pressure wavenumber spectra at $\omega\delta^*/U_0 = 1$ for $x_2 = 0.05\delta$, anisotropic turbulence (a-c) vs. isotropic turbulence (d-f); (a,d) Φ_{22}; (b,e) $\frac{k_1^2}{k^2}e^{-2|k|x_2}\Phi_{22}$; (c,f) $\frac{k_1^2}{k^2}e^{-2|k|x_2}\Phi_{22}\phi_m$.

direction.

IV. Conclusion

Wall pressure fluctuations were calculated using TNO-Blake model with input parameters provided by RANS results. Two zero pressure gradient (ZPG) flows with different Reynolds numbers and one adverse

pressure gradient (APG) flow were studied. The one-point spectra and the contribution from individual wall-normal positions across the turbulent boundary layer (TBL) were analyzed. The convection velocity and coherence length were calculated based on the obtained wavenumber spectra. The calculated results for both one- and two-point statistics agree with the literature. The Reynolds number and APG effects are well predicted. Furthermore, different formulations for the velocity spectrum and moving axis spectrum were applied to investigate the effect of length and time scales on the wall pressure fluctuations.

The major findings of this work are summarized as follows:

- The results show that the buffer layer contributes significantly to the ZPG wall pressure fluctuations over the entire frequency range, agreeing with the measurement results.[8,9] Larger temporal turbulence decay increases the contribution from the buffer layer to low frequencies. Consequently, the low-frequency slope becomes flatter and departs from the classic ω^2 increase.[16] Furthermore, the increased turbulence decay can significantly reduce the streamwise coherence length.

- The source map reveals that the source ridge contributed to the overlap region of the ZPG wall pressure spectra[1] ends at similar x_2^+ values. A larger Reynolds number shifts the source ridge to a higher frequency, which may result in an extended overlap range. Furthermore, the log region becomes more important with an increasing Reynolds number, which may be a reason for the increased coherence lengths.

- The APG significantly increases the contribution from the outer layer, which causes a steeper mid-frequency roll-off of the APG wall pressure spectra compared to the ZPG spectra. The smaller time scale across TBL may explain the reduced streamwise coherence length.

Acknowledgments

This work was supported through joint funding of DLR and Airbus.

References

[1]Goody, M. C., "Empirical Spectral Model of Surface Pressure Fluctuations," *AIAA Journal*, Vol. 42(9), 2004, pp. 1788–1794.

[2]Salze, E., Bailly, C., Marsden, O., Jondeau, E., and Juvé, D., "An experimental characterisation of wall pressure wavevector-frequency spectra in the presence of pressure gradients," *AIAA Paper 2014-2909*, 2014.

[3]Catlett, M. R., Anderson, J. M., Forest, J. B., and Stewart, D. O., "Empirical modeling of pressure spectra in adverse pressure gradient turbulent boundary layers," *AIAA Journal*, Vol. 54(2), 2016, pp. 569–587.

[4]Hu, N. and Herr, M., "Characteristics of wall pressure fluctuations for a flat plate turbulent boundary layer with pressure gradients," *AIAA Paper 2016-2749*, 2016.

[5]Rozenberg, Y., Robert, G., and Moreau, S., "Wall-pressure spectral model including the adverse pressure gradient effects," *AIAA Journal*, Vol. 50(10), 2012, pp. 2168–2179.

[6]Lee, S., "Empirical Wall-Pressure Spectral Modeling for Zero and Adverse Pressure Gradient Flows," *AIAA Journal*, Vol. 56(5), 2018, pp. 1818–1829.

[7]Hu, N., "Empirical model of wall pressure spectra in adverse pressure gradients," *AIAA Journal*, Vol. 56 (9), 2018, pp. 3491–3506.

[8]Blitterswyk, J. V. and Rocha, J., "An experimental study of the wall-pressure fluctuations beneath low Reynolds number turbulent boundary layers," *J. Acoust. Soc. Am.*, Vol. 141(2), 2017, pp. 1257–1268.

[9]Szőke, M., Fiscaletti, D., and Azarpeyvand, M., "Influence of boundary layer flow suction on trailing edge noise generation," *J. Sound Vib.*, Vol. 475, 2020, pp. 1–18.

[10]Corcos, G. M., "The Structure of the Turbulent Pressure Field in Boundary Layer Flows," *J. Fluid Mech.*, Vol. 18, 1964, pp. 353–378.

[11]Smol'yakov, A. and Tkachenko, V., "Model of a field of pseudosonic turbulent wall pressures and experimental data," *Akust. Zh.*, Vol. 37, 1991, pp. 1199–1207.

[12]Hu, N., "Coherence of wall pressure fluctuations in zero and adverse pressure gradients," *J. Sound Vib.*, Vol. 116316, 2021, pp. 1–27.

[13]Wilby, J. F. and Gloyna, F. L., "Vibration measurements of an airplane fuselage structure," *J. Sound Vib.*, Vol. 23(4), 1972, pp. 443–466.

[14]Hu, N., Buchholz, H., Herr, M., Spehr, C., and Haxter, S., "Contributions of Different Aeroacoustic Sources to Aircraft Cabin Noise," *AIAA Paper 2013-2030*, 2013.

[15]Smol'yakov, A., "A new model for the cross spectrum and wavenumber-frequency spectrum of turbulent pressure fluctuations in a boundary layer," *Acoustical Physics*, Vol. 52(3), 2006, pp. 331–337.

[16]Blake, W. K., *Mechanics of flow-induced sound and vibration*, Academic Press, Inc., 1986.

[17]Parchen, R., "Progress report DRAW : a prediction scheme for trailing edge noise based on detailed boundary layer characteristics," Tech. Rep. HAG-RPT-980023, TNO Institute of Applied Physics, The Netherlands, 1998.

[18]Panton, R. L. and Linebarger, J. H., "Wall pressure spectra for equilibrium boundary layers," *J. Fluid Mech.*, Vol. 65, 1974, pp. 261–287.

[19]Peltier, L. and Hambric, S., "Estimating turbulent-boundary-layer wall-pressure spectra from CFD RANS solutions," *Journal of Fluids and Structures*, Vol. 23, 2007, pp. 920–937.

[20]Bertagnolio, F., Fischer, A., and Zhu, W. J., "Tuning of turbulent boundary layer anisotropy for improved surface pressure and trailing-edge noise modeling," *J. Sound Vib.*, Vol. 333, 2014, pp. 991–1010.

[21]A. Fischer, F. Bertagnolio, H. M., "Improvement of TNO type trailing edge noise models," *International Symposium on Transport Phenomena and Dynamics of Rotating Machinery*, 2016.

[22]Stalnov, O., Paruchuri, C., and Joseph, P., "Towards a non-empirical trailing edge noise prediction model," *J. Sound Vib.*., Vol. 372, 2016, pp. 50–68.

[23]Bailly, C. and Juvé, D., "A stochastic approach to compute subsonic noise using linearized Euler's equations," *AIAA Paper 1999-1872*, 1999.

[24]Grasso, G., Jaiswal, P., Wu, H., Moreau, S., and Roger, M., "Analytical models of the wall-pressure spectrum under a turbulent boundary layer with adverse pressure gradient," *J. Fluid Mech.*, Vol. 877, 2019, pp. 1007–1062.

[25]Taylor, G., "The spectrum of turbulence," *Proc. R. Soc. Lond.*, Vol. 164(919), 1938, pp. 476–490.

[26]Tam, C. K. W. and Auriault, L., "Jet mixing noise from fine-scale turbulence," *AIAA Journal*, Vol. 37(2), 1999, pp. 145–153.

[27]Ewert, R., Dierke, J., Siebert, J., Neifeld, A., Appel, C., Siefert, M., and Kornow, O., "CAA broadband noise prediction for aeroacoustic design," *J. Sound Vib.*, Vol. 330, 2011, pp. 4139–4160.

[28]Hu, N., Reiche, N., and Ewert, R., "Simulation of turbulent boundary layer wall pressure fluctuations via Poisson equation and synthetic turbulence," *J. Fluid Mech.*, Vol. 826, 2017, pp. 421–454.

[29]Hu, N., Appel, C., Haxter, S., Callsen, S., and Klabes, A., "Simulation of Surface Pressure Fluctuations on an Airbus-A320 Fuselage at Cruise Conditions," *AIAA Journal*, Vol. 059284, 2020, pp. 1–13.

[30]Kim, J., "Propagation velocity of perturbations in turbulent channel flow," *Phys. Fluids A*, Vol. 5(3), 1993, pp. 695–706.

[31]Del Alámo, J. C. and Jiménez, J., "Estimation of turbulent convection velocities and corrections to Taylor's approximation," *J. Fluid Mech.*, Vol. 640, 2009, pp. 5–26.

[32]Togiti, V. and Eisfeld, B., "Assessment of g-Equation Formulation for a Second-Moment Reynolds Stress Turbulence Model," *AIAA Paper 2015-2925*, 2015.

[33]Hu, N., Reiche, N., and Ewert, R., "Numerical investigation of wall pressure fluctuations for zero and adverse pressure gradient turbulent boundary layers using synthetic anisotropic turbulence," *AIAA Paper 2017-3200*, 2017.

[34]Erbig, L. and Lardeau, S., "Hybrid RANS/LES of an Adverse Pressure Gradient Turbulent Boundary Layer Using an Elliptic Blending Reynolds Stress Model and Anisotropic Linear Forcing," *Progress in Hybrid RANS-LES Modelling*, 2019, pp. 73–84.

[35]Hu, N. and Erbig, L., "Effect of Sensor Mounting and Flow History on Measured Wall Pressure Spectra," *AIAA Journal*, Vol. 58 (7), 2020, pp. 2964–2974.

[36]Jaiswal, P., Moreau, S., Avallone, F., Ragni, D., and Pröbsting, S., "On the use of two-point velocity correlation in wall-pressure models for turbulent flow past a trailing edge under adverse pressure gradient," *Phys. Fluids*, Vol. 32, 2020, pp. 1–27.

[37]Cohen, E. and Gloerfelt, X., "Influence of pressure gradients on wall pressure beneath a turbulent boundary layer," *J. Fluid Mech.*, Vol. 838, 2018, pp. 715–758.